ORIGINAL ARTICLE

International Journal of Applied Mathematics in Control Engineering

Journal homepage: http://www.ijamce.com

Pivotal technology research for the Design of High-Speed Permanent Magnet Motor Rotor Structures in Military Mobile Power Stations

Qingyi Kong[1,2] | Shengyan Zhou[1] | Yuhui Fan[1] | Zida Hao[1] | Ye Rong[1]*

[1]Hebei Jiaotong Vocational and Technical College, Shijiazhuang 050035, China

[2]Moons' Industries (Taicang) Co., Ltd., Suzhou 215400, China

Correspondence
Ye Rong, PhD, Hebei Jiaotong Vocational and Technical College, Shijiazhuang 050035, China
Email: rongye1983@hejtxy.edu.cn

Article Info
Article history:
Received 24 January 2026
Accepted 15 March 2026
Available online 16 March 2026

Abstract

The military mobile power station employs micro gas turbine (MGT) technology, which offers advantages such as low noise, high efficiency, minimal vibration, and reduced emissions. The core component and key enabling technology within the MGT system is the high-speed permanent magnet machine. In the design of ultra-high-speed permanent magnet motors, two primary rotor configurations are commonly studied: the three-layer surface-mounted rotor and the solid cylindrical rotor. Accordingly, this paper presents a comparative design and theoretical analysis of ultra-high-speed permanent magnet motors with these two distinct rotor configurations. Through prototype testing, the influence of rotor structure on motor performance is examined.

KEYWORDS

Military mobile power station, micro gas turbine, high-speed permanent magnet motor, rotor structure, rotor strength, rotor dynamics, losses

1 | INTRODUCE

The continuous advancement of key technologies, such as high-speed bearings, high-speed permanent magnet motors, and efficient regenerative heat exchangers, has driven the maturation of micro gas turbine (MGT) systems. These systems effectively address the limitations associated with conventional internal combustion engines commonly deployed in military mobile power stations, including excessive noise, limited service life, pronounced vibration, high emissions, and insufficient reliability [1]. Consequently, the performance of military mobile power stations can be substantially improved. In a typical MGT, the high-speed permanent magnet motor is directly coupled to the compressor and turbine, eliminating the need for a gear reducer [2]. During operation, the motor drives the impeller to rotate, thereby compressing the air. After passing through a recuperator, the compressed air enters the combustion chamber, where ignition produces high-temperature gas that drives the turbine, after which the permanent magnet motor transitions to power generation mode.

Since the mid-1990s, Capstone Turbine Corporation in the United States has successively introduced MGT products with rated powers of 30 kW, 60 kW, and 200 kW [3]. Later, using the 200 kW unit as a modular building block, the company achieved

Digital Object Identifiers: 10.62953/IJAMCE.883080

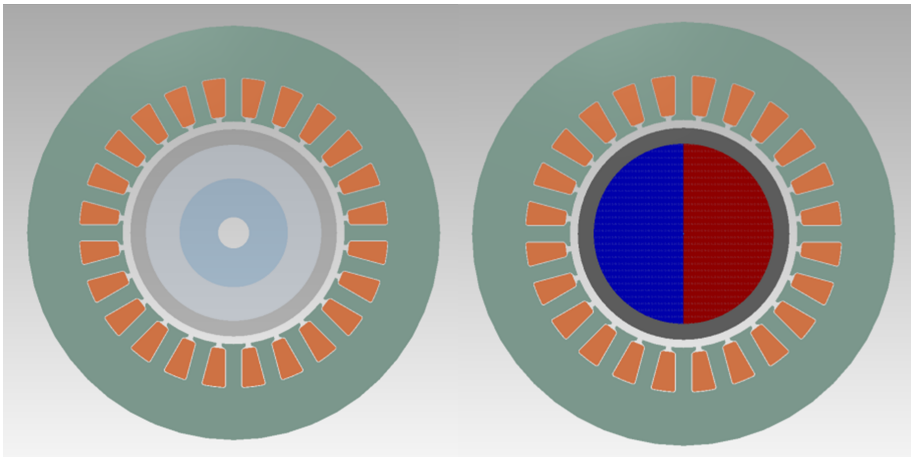


FIGURE 1 Two types of rotor structure motor simulation models.

grid-connected power generation systems with capacities of 600 kW, 800 kW, and 1 MW.

Based on the arrangement of permanent magnets within the rotor, rotor configurations are generally categorized into two types [4]: interior-mounted and surface-mounted (Figure 1). Differences in rotor topology directly influence the rotor's stress distribution. Investigating the effects of rotor structure on electromagnetic performance, thermal management, mechanical strength, and critical speed has therefore become a central focus in the research and development of high-speed permanent magnet motors.

2 | MOTOR STRUCTURE AND BASIC PARAMETERS

To investigate the impact of rotor structure on motor performance, this study designed and compared two ultra-high-speed permanent magnet motors. One motor features a three-layer surface-mounted permanent magnet rotor, while the other uses a solid cylindrical permanent magnet rotor. Both rotors are sleeved with GH4169 alloy. For a clear performance comparison, the two motors share the same rated voltage, output power, and rotational speed. The motor configurations are illustrated in Figure 1, and the design parameters are summarized in Table 1.

TABLE 1 Basic parameters of motor design.

Name of Parameter	Rotor Configuration	
	Three-layer surface-mounted	Solid cylindrical
Rated Power / kW	100	100
Rated Speed / (r/min)	45000	45000
Number of stator slots	24	24
Number of pole-pairs	1	1
Stator outer diameter / mm	160	160
Rotor outer diameter / mm	80	80
Gas length / mm	3	3
Sheath thickness / mm	6	6
Length of permanent magnet / mm	255	204



FIGURE 2 The magnetic flux density of the air gap of the two types of motors.

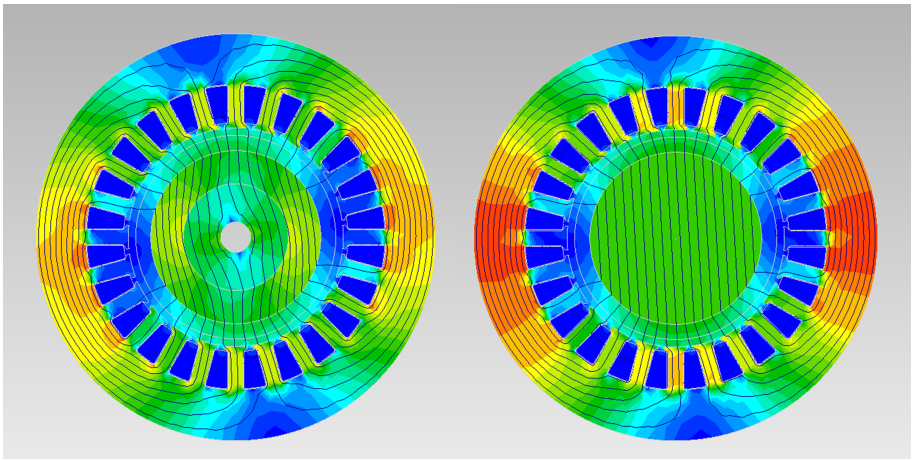


FIGURE 3 The magnetic flux density distribution of the two types of motors.

3 | ANALYSIS OF AIR-GAP MAGNETIC FLUX DENSITY AND MAGNETIC FIELD

Simulations were performed to analyze the air-gap magnetic flux density and losses of both motor types under identical electrical excitation. The results are presented in Figure 2.

The amplitude of the air-gap flux density is 0.557 T for the three-layer surface-mounted rotor motor, compared to 0.696 T for the solid rotor motor. Although the solid rotor motor exhibits a higher flux density, the waveforms of the two designs are similar. The permanent magnet mass is 4.75 kg in the three-layer surface-mounted rotor and 6.15 kg in the solid rotor, indicating that the solid rotor configuration supplies a stronger excitation magnetic field.

The magnetic field analysis results are given in Figure 3. The stator core flux density reaches 1.45 T in the solid rotor motor, whereas it is 1.14 T in the three-layer surface-mounted rotor motor.

4 | COMPARISON AND ANALYSIS OF ROTOR STRENGTH AND CRITICAL SPEED FOR TWO MOTOR STRUCTURES

In high-speed permanent magnet motors, rotor strength and critical speed are key design considerations. The rotor structure, the mechanical properties of its components, and their mutual interactions significantly influence both strength and critical speed. This paper compares two rotor configurations: the three-layer surface-mounted rotor and the solid cylindrical permanent

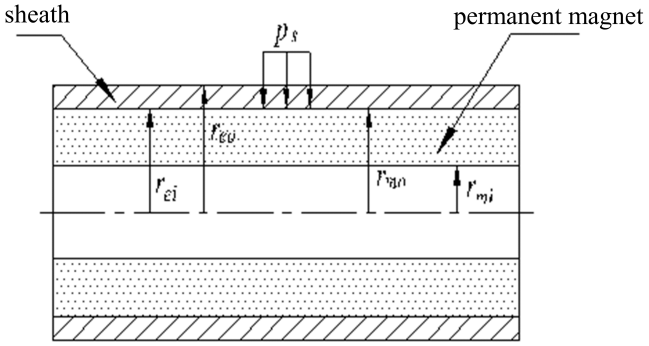


FIGURE 4 Permanent magnet stress analysis model.

magnet rotor. The analysis assumes a rotor temperature of 160 °C and fully accounts for the safety margins of each mechanical component.

Special attention is given to the interference fit between the retaining sleeve and the permanent magnet. Excessive interference may induce cracks in the magnet during assembly, compromising rotor stability and potentially leading to rotor burst. Conversely, insufficient interference prevents adequate pressure from developing between the sleeve and the magnet, causing the sleeve to lose its protective function.

Additionally, the design requires that the first-order bending critical speed exceed 1.26 times the rated speed. This ensures that the high-speed permanent magnet rotor operates as a rigid rotor under rated conditions.

TABLE 2 Material properties.

Property (Material)	GH4169	Sm_2Co_{17}	Al17075	40CrNiMoA
Density / $g\,cm^{-3}$	8.24	8.4	2.85	7.83
Elastic modulus / GPa	204	117	74	209
Poisson's ratio	0.3	0.28	0.33	0.3
Linear expansion coefficient (20–100°C) / $10^{-6}\,K^{-1}$	11.8	8	23.9	12.8
Yield strength / MPa	1030	85	460	835

4.1 | Rotor strength analysis

The high-speed permanent magnet motor presented in this work employs cylindrical Sm_2Co_{17} permanent magnets and a GH4169 alloy retaining sleeve. Because the permanent magnets are brittle, the first strength theory is adopted to assess their mechanical strength and prevent fracture [5]. In contrast, the sleeve is a ductile material; therefore, the fourth strength theory is applied to avoid plastic deformation and structural failure [6]. A simplified stress analysis model is shown in Figure 4.

In the model, r_{mi} and r_{mo} denote the inner and outer radii of the permanent magnet, while r_{ei} and r_{eo} represent the inner and outer radii of the sleeve, respectively.

First, the interference between the permanent magnet and the sheath is calculated using Equation (1).

$$\delta = \delta_s - \Delta\delta_d - u_{t,ei} \tag{1}$$

Here, δ_s, $\Delta\delta_d$, and $u_{t,ei}$ represent the static interference, rotational interference, and temperature interference, respectively. Therefore, the static pressure between the permanent magnet and the housing can be calculated, including the assembly pressure P_s and the working static pressure P , as given by Equation (2).

$$\begin{aligned} P_s &= \frac{\delta_s}{r_i[\frac{1}{E_m}\frac{r_o^2+r_i^2}{r_o^2-r_i^2} - V_m + \frac{1}{E_e}\frac{r_o^2+r_i^2}{r_o^2-r_i^2} - V_e]} \\ P &= \frac{\delta}{r_i[\frac{1}{E_m}\frac{r_o^2+r_i^2}{r_o^2-r_i^2} - V_m + \frac{1}{E_e}\frac{r_o^2+r_i^2}{r_o^2-r_i^2} - V_e]} \end{aligned} \tag{2}$$

Finally, the static pressure δ_{m,r_4} of the permanent magnet and the working stress are determined, as expressed in Equation (3).

$$\begin{aligned} \delta^s_{m,r_4} &= \sqrt{\frac{1}{2}\left[(\delta^s_r - \delta^s_\theta)^2 + (\delta^s_r)^2 + (\delta^s_\theta)^2\right]} \\ \delta^d_{m,r_4} &= \sqrt{\frac{1}{2}\left[(\delta^d_r - \delta^d_\theta)^2 + (\delta^d_r)^2 + (\delta^d_\theta)^2\right]} \end{aligned} \tag{3}$$

$$\begin{aligned} \delta^d_r &= \delta^d_{r,1} + \delta^d_{r,2} \\ \delta^d_\theta &= \delta^d_{\theta,1} + \delta^d_{\theta,2} \end{aligned} \tag{4}$$

Here, δ^s_r and δ^s_θ represent the radial and tangential static assembly stresses, respectively. Meanwhile, $\delta^d_{r,1}$ and $\delta^d_{r,2}$ denote the radial working assembly stresses, and $\delta^d_{\theta,1}$ and $\delta^d_{\theta,2}$ correspond to the rotational radial and tangential stresses.

The same analytical method is applied to assess the sleeve strength against the design requirements. The rotor operating conditions are listed in Table 3. The corresponding simulation results are shown in Figure 5.

TABLE 3 Rotor operating conditions.

condition-name	Working Condition
The Interference Fit between the Sheath and the Permanent Magnet Diameter(mm)	0.236
Working Speed(r/min)	45000
Operating Temperature(°C)	160
Initial Environmental Eemperature(°C)	20

As shown in Figure 5, different rotor structures produce distinct stress distributions. The stress in the outer sheath is similar for both designs. However, for the three-layer surface-mounted magnetic steel, the tensile stress is relatively low, while the compressive stress is significantly higher. Meanwhile, the contact pressure between the permanent magnets and the outer sheath remains comparable across both configurations.

4.2 | Critical speed analysis

A finite element model of the high-speed permanent magnet motor rotor was developed using Ansys software. A photograph of the rotor is presented in Figure 6. The governing equation for calculating the system's critical speed is given by Equation (5).

$$\left(\mathbf{K}_{xz} - \omega_i^2 \mathbf{M}_{xz}\right)\mathbf{y}_i = \mathbf{0} \tag{5}$$

Here, $\mathbf{K}_{xz}$ is the stiffness matrix of the rotor system; $\mathbf{M}_{xz}$ is the mass matrix of the rotor system; ω_i is the i-th natural angular frequency of the rotor system; $\mathbf{y}_i$ corresponds to the i-th mode shape associated with ω_i. The i-th critical speed in revolutions per

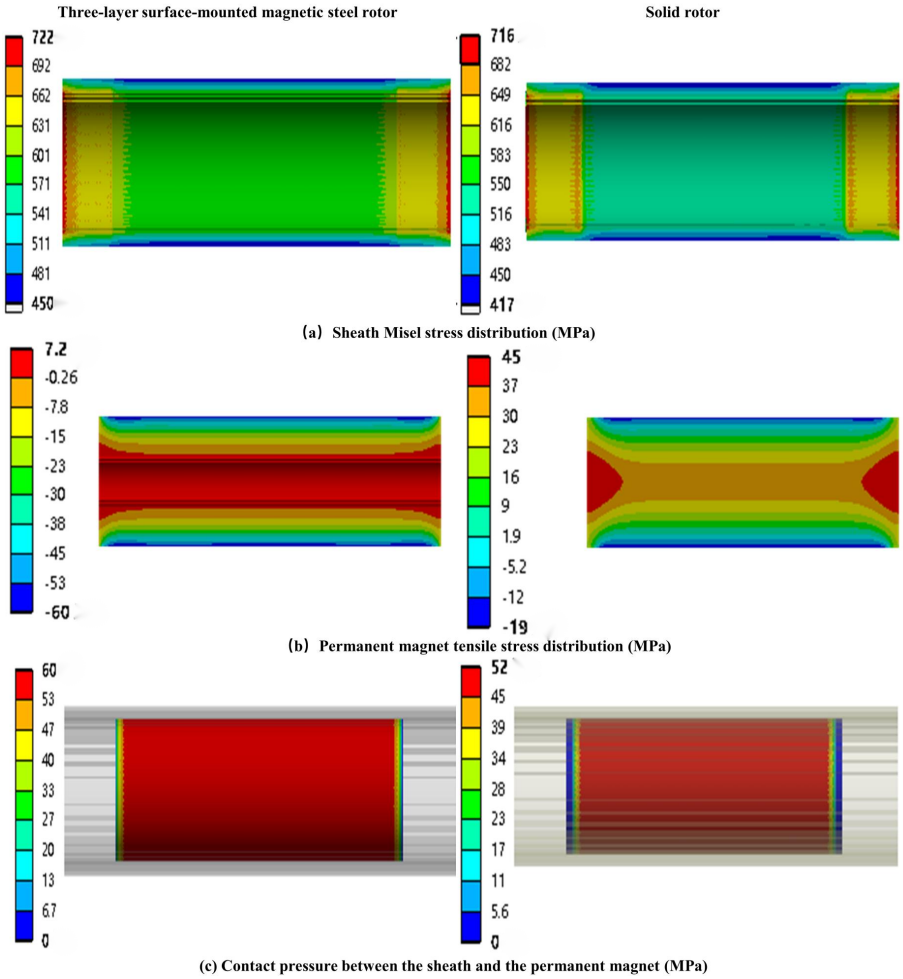


FIGURE 5 Stress distribution map.

minute is obtained as $N_{\mathrm{cr},i} = \frac{60}{2\pi}\omega_i$.

To achieve a reasonable distribution of critical speeds and satisfy rotor-dynamics requirements [7], squirrel-cage elastic supports were installed at both the front and rear bearings of the rotor. Eight sets of stiffness values ranging from 5×10^5 N/m to 5×10^7 N/m were selected for comparing their dynamic characteristics.

The results show that although the two rotor structures exhibit different critical speeds, their first three vibration modes are identical. The first critical speed corresponds to a conical rigid-body mode, the second to a cylindrical rigid-body mode, and the third to the first bending mode. When the operating speed approaches a critical speed, the rotor enters resonance. Under low damping, this can generate excessive vibration stress, leading to rotor bending, bearing damage, and other failures.

The designed permanent-magnet motor operates at a rated speed of 45000 r/min, which lies between the second and third critical speeds. Its maximum speed remains below the third critical speed. The analysis further indicates that, owing to its shorter span and lower mass, the solid rotor exhibits a slightly higher first-bending critical speed than the three-layer surface-mounted rotor, making it more suitable for stable high-speed operation.

4.3 | Rotor loss analysis

The rotor losses in high-speed permanent magnet motors comprise eddy-current losses and wind-age losses. These motors are compact, which complicates heat dissipation [8]. Increased losses and the associated temperature rise can cause the rotor to expand and lengthen, potentially loosening the insulation jacket. In severe cases, demagnetization of the permanent magnets may occur. Therefore, accurate estimation of rotor losses during the design stage is essential to ensure stable motor operation.

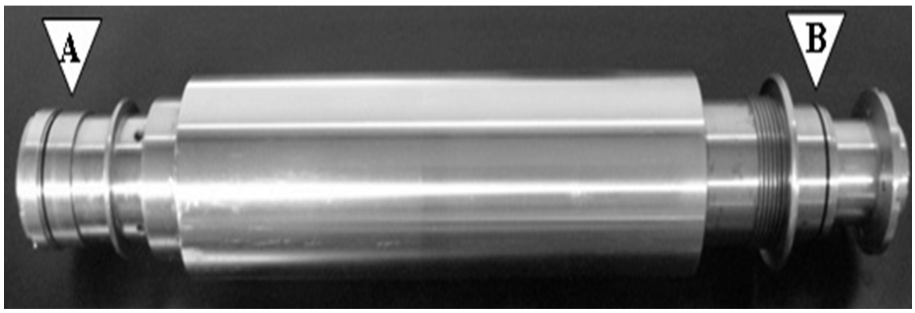


FIGURE 6 Stress distribution map.

4.3.1 | Rotor friction loss

Wind-age loss arises from the relative motion between the rotor and the surrounding air. This loss increases with rotational speed and is influenced by the rotor surface roughness, the rotational speed itself, and the properties of the ambient gas medium, as given in Equation (6).

$$P = kC_f \pi \rho \omega^3 r^4 l \tag{6}$$

Here, k denotes the rotor surface roughness coefficient (for a smooth surface, $k = 1$). The variable ρ represents air density, while ω, r, and l correspond to the angular velocity, rotor radius, and axial length, respectively. The coefficient C_f describes the air friction, which depends on the rotor surface shear stress. Equation 6 is mainly applicable for qualitative analysis of rotor windage loss. Accurate quantitative evaluation requires a three-dimensional field analysis.

Basic equations and solution model

Based on viscous fluid mechanics [9], the fluid flow around the rotor of a high-speed permanent magnet motor can be described three-dimensionally. Using air as the cooling medium, the governing equations are derived from the time-averaged continuity equation, the instantaneous Navier–Stokes equations, and the Reynolds-averaged equations (7) - (9).

$$\begin{aligned} \frac{\partial \overline{u}_i}{\partial x_i} &= 0 \\ \frac{(\partial u_i)'}{\partial x_i} &= 0 \end{aligned} \tag{7}$$

$$\rho \frac{\partial u_i}{\partial t} + \rho u_j \frac{\partial u_i}{\partial x_j} = \rho F_i - \frac{\partial p}{\partial x_i} + u \frac{\partial^2 u_i}{\partial^2 x_j} \tag{8}$$

$$\rho \frac{\partial \overline{u}_i}{\partial t} + \rho \overline{u}_j \frac{\partial u_i}{\partial x_j} = \rho \overline{F}_i - \frac{\partial \overline{p}}{\partial x_i} + \frac{\partial}{\partial x_j}(u \frac{\partial \overline{u}_i}{\partial x_j} - \rho u_i' u_j') \tag{9}$$

Here, $\overline{u}_i$ denotes the time-averaged flow velocity, while u_i' represents the fluctuating component; F_i corresponds to the body force, and $\overline{p}$ is the time-averaged pressure. Here the indices i and j take values x, y, z with $i \neq j$. The fluid properties are described by the dynamic viscosity μ and the density ρ.

The windage loss in high-speed permanent-magnet motors originates primarily from viscous friction between the rotor surface and the narrow air gap. This loss mechanism depends directly on the velocity and pressure distributions of the fluid within the gap

[10]. Three key factors govern the flow field in the air gap: 1) Tangential flow driven by rotor rotation; 2)Axial flow of the cooling fluid; 3)Centrifugal effects due to high-speed rotation, which can lead to the formation of Taylor vortices.

When gravitational effects on the air are neglected, a renormalization-group (RNG) based turbulence model provides a suitable framework for solving the instantaneous Navier–Stokes equations in this configuration.

$$\rho\frac{\partial k}{\partial t}+\rho u_i\frac{\partial k}{\partial x_i}=\frac{\partial}{\partial x_j}[(\mu+\frac{u_t}{\partial\sigma_k})\frac{\partial k}{\partial x_j}]+G_k+\rho\varepsilon \tag{10}$$

$$\rho\frac{\partial s}{\partial t}+\rho u_i\frac{\partial s}{\partial x_i}=\frac{\partial}{\partial x_j}[(\mu+\frac{u_t}{\partial\sigma_\varepsilon})\frac{\partial \varepsilon}{\partial x_j}]+C_1sG_k\frac{s}{k}+C_2s\rho\frac{s^2}{k} \tag{11}$$

Here, G_k represents the turbulent kinetic energy generated by the mean-velocity gradient; σ_k and σ_ε are the effective turbulent Prandtl numbers for the turbulent kinetic energy k and its dissipation rate ε, respectively; and μ_t denotes the turbulent viscosity, given by $\mu_t=\rho C_\mu k^2/\varepsilon$. The constants $C_{2\varepsilon}$, C_μ, σ_k, and σ_ε take the values 1.68, 0.0085, 0.7179, and 0.7169, respectively [11, 12, 13]. The coefficient $C_{1\varepsilon}$ depends on the flow conditions and is defined by the following solution model:

$$C_1s=1.42-\frac{\eta(1-\frac{\eta}{\eta_0})}{1+\beta\eta^2} \tag{12}$$

$$\eta=Sk/\varepsilon \tag{13}$$

Here, $S=(2S_i^2)^{\frac{1}{2}}$, where S_i represents the time-averaged strain rate of the fluid; η_0 and β are constants, with values of 4.38 and 0.015 respectively.

Boundary conditions and calculation of wind friction loss

A fluid field analysis was conducted on the rotor surface wind friction loss of the high-speed permanent magnet synchronous motor under rated conditions. During the fluid field analysis, the following assumptions were made:

1. The fluid enters the wind path perpendicularly to the inlet surface;
2. The rotor loss is carried out by the fluid through the outlet of the wind path in the form of heat.
3. The boundary conditions of the 3D fluid field model are as follows: (i) The fluid inlet is designated as the velocity inlet, the outlet is designated as the pressure outlet, and the fluid outlet pressure is set to atmospheric pressure; (ii)The permanent magnets, insulation sleeves, air gaps, and stators are designated as periodic boundary conditions; (iii)The motion boundary is the interface between the insulation sleeve and the air gap, and the rotational speed and roughness of the rotor and stator are specified on this interface. (iv)The interface between the solid and the fluid is set as a coupled boundary; (v)Other boundaries are considered as adiabatic boundaries.

Based on the above settings, a fluid field analysis model for the solid rotor motor was established. The rotor wind friction loss of the high-speed permanent magnet motor can be obtained by calculating the total energy change of the high-speed permanent magnet motor.

The factors influencing rotor frictional losses

Based on the calculation of the fluid field of rotor wind friction loss in high-speed permanent magnet motors, it is known that the relationship between rotor wind friction loss and the rotational speed of the high-speed permanent magnet motor can be expressed as:

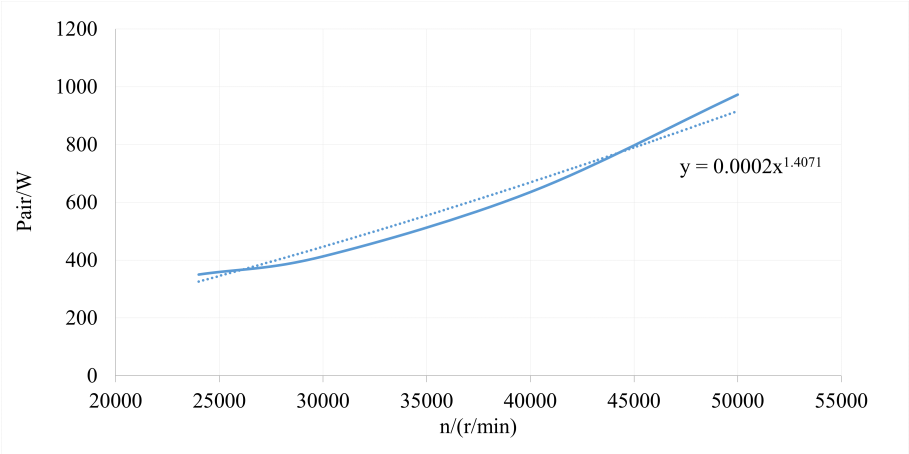


FIGURE 7 The relationship between wind friction loss and rotational speed.

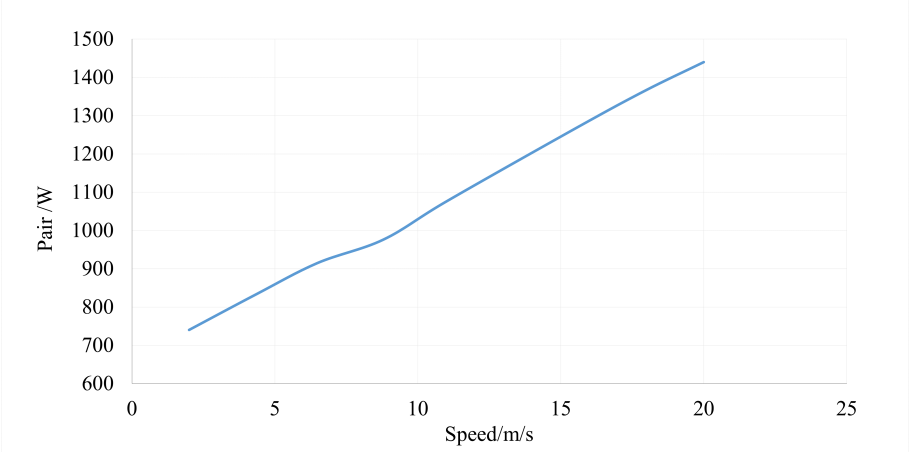


FIGURE 8 Axial wind speed and loss relationship curve.

$$P_a = kn^{\alpha} \tag{14}$$

Here, n represents the rotor speed; k and α are undetermined coefficients. Through nonlinear data fitting, the power exponent α can be obtained as 1.4071. The fitting curve is shown in Figure 7. The rotor wind friction loss is related to the motor speed, stator slot opening, stator slot filling rate, rotor surface roughness, and axial wind speed. Based on the analysis of the fluid field, the influence of axial wind speed and rotor surface roughness on rotor wind friction loss is shown in Figure 8 and 9. It increases the axial wind speed is beneficial for heat dissipation, but it increases the wind friction loss. To reduce the rotor wind friction loss of high-speed permanent magnet motors, the axial wind speed should be optimized and the height of rotor surface rough particles should be improved.

4.3.2 | Rotor eddy-current loss

The main causes of rotor eddy current loss are as follows: 1) The slotting on the stator surface leads to changes in the air-gap magnetic permeability, causing changes in the magnetic circuit during rotor rotation, which in turn leads to periodic changes in the magnetic field and thereby triggering eddy currents and losses. 2) The time harmonics of the stator windings cause eddy currents and losses in the rotor, which are determined by the control method of the frequency converter; 3) It is caused by the spatial harmonics of the current, which depends on the specific form of the windings. According to the Poynting theorem, the

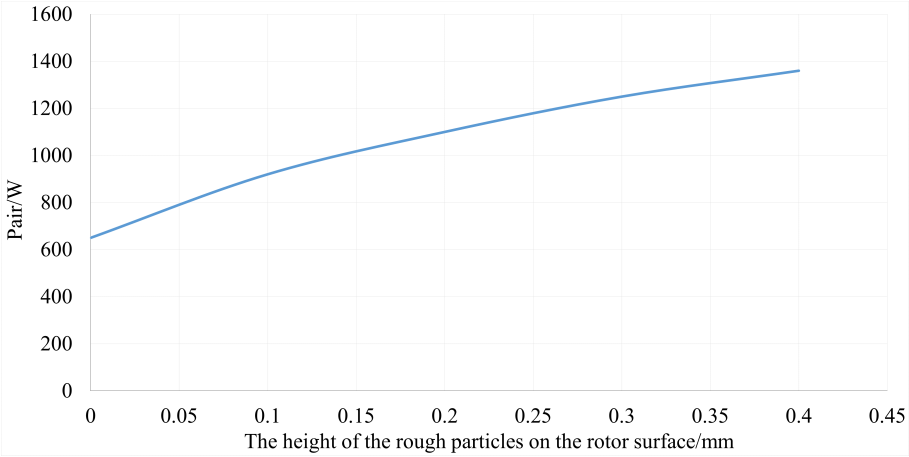


FIGURE 9 The curve showing the relationship between the height of rough particles on the rotor surface and the loss.

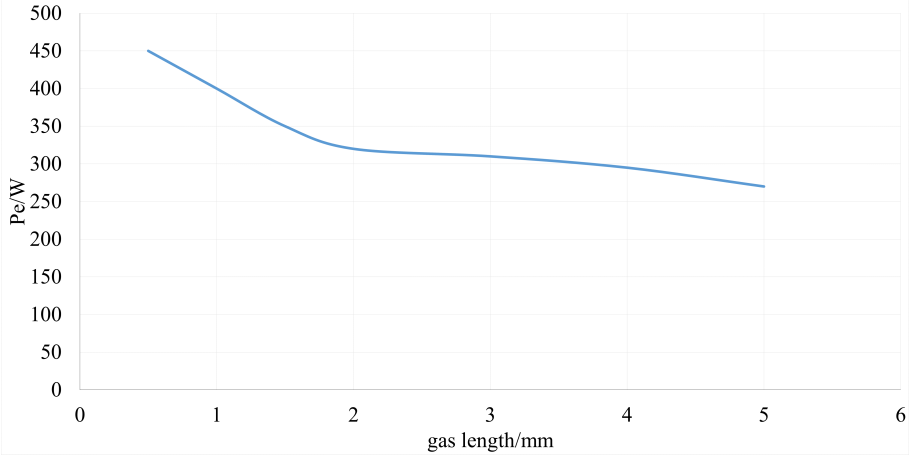


FIGURE 10 Rotor eddy current losses with different air gap lengths.

eddy current losses of each part can be calculated. To facilitate the calculation, when using the analytical method to calculate the rotor eddy current loss, the stator winding current is often equivalent to a surface current, and the saturation of the core, leakage magnetic flux and hysteresis effect are ignored [14]. It is assumed that the electrical conductivity and magnetic permeability of the materials of each structural component of the rotor are constants.

The finite element calculation method can take into account the influence of factors such as saturation, leakage magnetic flux, and material nonlinearity. Through calculation, it can be known that increasing the air-gap length can weaken the stator tooth harmonics and the high-order harmonics of the stator current, thereby reducing the rotor eddy current loss. However, increasing the air-gap length will cause the air-gap magnetic induction intensity to decrease. To meet the requirements of the motor output power, the amount of permanent magnets needs to be increased. Considering the air-gap size, the range before the trend of the decrease in eddy current loss slows down should be selected. The relationship curve between eddy current loss and air-gap length is shown in Figure 10.

5 | EXPERIMENTAL STUDY

The prototype of the high-speed permanent magnet motor is shown in Figure 11. The variation with rotational speed of the effective values of the vibration acceleration of the casing and the vibration amplitude at the shaft neck during the motor's speed increase process with elastic damping support (Figure 12 and 13).

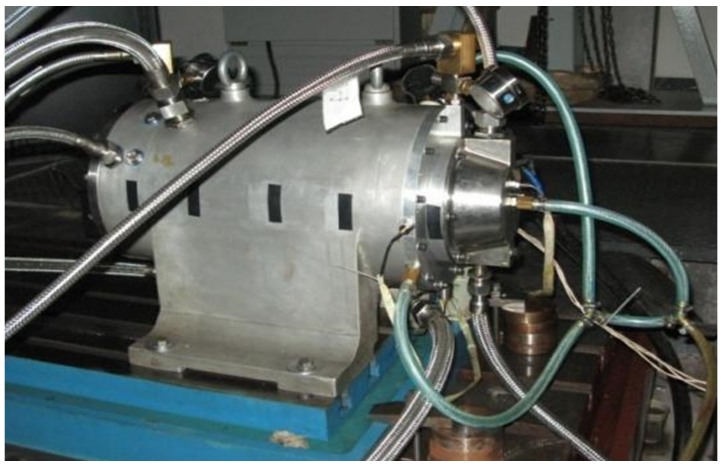


FIGURE 11 High-speed permanent magnet motor prototype.

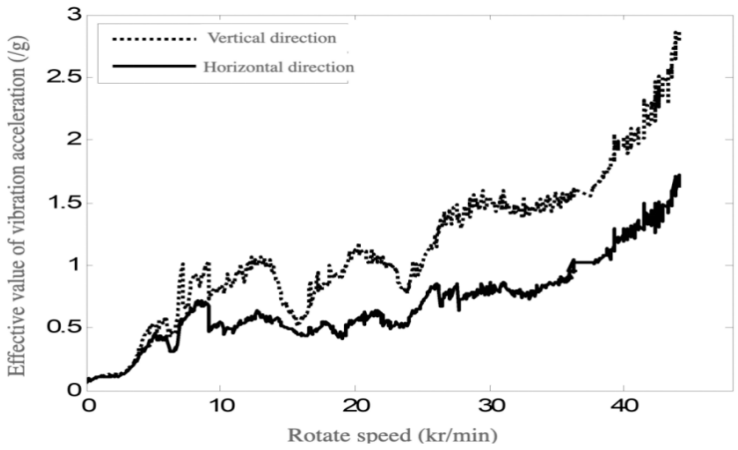


FIGURE 12 The effective value of the machine casing vibration acceleration varies with the rotational speed.

When the motor's rotational speed is around 12000 r/min and 21000 r/min, the motor vibration acceleration reaches its peak, and it is close to the critical rotational speed of rigid body translation and the critical rotational speed of rigid body rotation (Figure 12). It is preliminarily judged that this is caused by resonance when the over-limit condition is reached. However, due to the good damping effect of the damper, the system can smoothly pass through the critical rotational speed, and the vibration acceleration decreases significantly after each passage of the critical speed. As the rotational speed increases, the vibration acceleration of the casing continues to increase until the working rotational speed of 45000 r/min, and the peak value does not exceed 3g.

From Figure 13 , it can be seen that the amplitude at the shaft neck is the largest at low speeds, reaching 70 μm. After the rotational speed exceeds 21000 r/min, it rapidly decreases to approximately 30 μm. During the process of further increasing the rotational speed to 45000 r/min, the vibration amplitude does not increase significantly. The motor rotor with elastic support and the compression oil film damper smoothly passes over its rigid body translation and cone motion modes and reaches the rated working speed of 45000 r/min.

6 | CONCLUSION

In order to compare and analyze the impact of rotor structure differences on the performance of the motor, this paper designs two three-layer surface-mounted rotor high-speed permanent magnet motors with the same stator structure, winding parameters



FIGURE 13 The effective value of the vibration amplitude at the journal varies with the rotational speed.

and rotor outer diameter, as well as a cylindrical permanent magnet rotor high-speed permanent magnet motor. The differences in electromagnetic, rotor strength, critical speed and rotor loss between the two rotor structures of the motors are compared and analyzed. The following conclusions are drawn:

1. The solid rotor has better strength. When operating at the same speed, the solid rotor permanent magnets are less likely to generate stress concentration, making it easier for the rotor to run stably;
2. Under the condition of meeting the rated performance requirements, the length of the solid motor rotor is shorter, which is conducive to reducing the rotor mass, lowering the rotor span, increasing the first-order bending speed of the rotor, and facilitating the stable operation of the rotor;
3. The rotor loss analysis results show that by controlling the cooling air volume and the height of the surface rough particles of the rotor, the rotor wind friction loss can be reduced, and selecting an appropriate air gap length can effectively reduce the rotor eddy current loss.

ACKNOWLEDGEMENTS

Acknowledgements should include contributions from anyone who does not meet the criteria for authorship (for example, to recognize contributions from people who provided technical help, collation of data, writing assistance, acquisition of funding, or a department chairperson who provided general support), as well as any funding or other support information.

CONFLICT OF INTEREST

You may be asked to provide a conflict of interest statement during the submission process. Please check the journal's author guidelines for details on what to include in this section. Please ensure you liaise with all co-authors to confirm agreement with the final statement.

AUTHOR CONTRIBUTIONS

Conceptualization, Q.-Y.K.and Y.R.; methodology, Y.R. and Z.-B.D.; software, L.-Y.S. and L.-Z.G.; validation, Q.Z., L.-Z.G. and G.-L.W.; formal analysis, L.-Z.G. and S.-Y.Z.; investigation, L.-Y.S. and S.-Y.Z.; resources, Q.-Y.K.; data curation, Z.-B.D. and S.-Y.Z.; writing—original draft preparation, Q.-Y.K.; writing—review and editing, Y.R., Q.Z. and Z.-B.D.; visualization, G.-L.W. and L.-Y.S.; supervision, G.-L.W.; project administration, L.-Z.G. and Q.Z.; funding acquisition, Z.-B.D. All authors have read and agreed to the published version of the manuscript.

FUNDING

This research was funded by Human Resources and Social Security in Hebei Province, grant number C2025030. This research was also supported by the Research Project for University Students of Hebei Jiaotong Vocational and Technical College, with grant numbers KJ-202510 and KJ-202511.

REFERENCES

[1] Horowitz, M. C.; Samotin, L. R. Driving Too Fast or Too Slow: Analyzing Military Adoption of the Combustion Engine. *SSRN Electronic Journal*, 2025. **[CrossRef]**

[2] Shen, Q.; Zhou, Z.; Li, S.; Liao, X.; Wang, T.; He, X.; Zhang, J. Design and Analysis of High-Speed Permanent Magnet Motors: A Review on the State of the Art. *Machines*, 2022, 10(7), 549. **[CrossRef]**

[3] Belrzaeg, M.; Sif, M. A.; Almabsout, E.; Benisheikh, U. A. Distributed Generation for Microgrid Technology. *International Journal of Scientific Research Updates*, 2023, 6(1), 083–092. **[CrossRef]**

[4] Rong, Y.; Kong, Q.; Liu, B.; Sun, Z.; Wang, G.; Li, Y. Study on Influence of Magnetic Properties of Ultrathin Unoriented Silicon Steel Sheet in Service. In Proceedings of the 2022 IEEE 5th International Electrical and Energy Conference (CIEEC), 2022, pp. 3798–3805. **[CrossRef]**

[5] Hu, K.; Zhang, G.; Zhang, W. Rotor Design and Optimization of High-Speed Surface-Mounted Permanent Magnet Motor Based on the Multi-Physical Field Coupling Method. *IEEE Access*, 2023, 11, 69614–69625. **[CrossRef]**

[6] Nazarenko, S.; Kovalenko, R.; Pobidash, A.; Kalynovskiy, A. Experimental Study of the Sleeve Material Mechanical Properties During the Sample Tensile Test. *Key Engineering Materials*, 2023, 952, 111–118. **[CrossRef]**

[7] Fazdi, M. F.; Hsueh, P.-W. Parameters Identification of a Permanent Magnet DC Motor: A Review. *Electronics*, 2023, 12(12), 2559. **[CrossRef]**

[8] Li, Z.; Wang, P.; Liu, L.; Xu, Q.; Che, S.; Zhang, L.; Du, S.; Zhang, H.; Sun, H. Loss Calculation and Thermal Analysis of Ultra-High Speed Permanent Magnet Motor. *Heliyon*, 2022, 8(11). **[CrossRef]**

[9] Luo, H.; Zhang, Y.; Wang, H.; Liu, G.; Zhang, F. Cooling Structure Design of High-Speed Permanent Magnet Synchronous Machine With Axial Ventilation Self-Cooling Rotor. *IEEE Access*, 2024, 12, 27005–27016. **[CrossRef]**

[10] Sukenik, J.; Toman, M.; Cipin, R.; Vitek, O. CFD-Based Estimation of Air-Gap Windage Losses in High-Speed Machines with Axial Flow. In Proceedings of the 2025 Energy Conversion Congress & Expo Europe (ECCE Europe), 2025, pp. 1–6. **[CrossRef]**

[11] Canet, L. Functional Renormalisation Group for Turbulence. *Journal of Fluid Mechanics*, 2022, 950, P1. **[CrossRef]**

[12] Gul, M. Z.; Yangaz, M. U.; Sen, S. A Two-Time-Scale Turbulence Model and Its Application in Free Shear Flows. *Applied Sciences*, 2024, 14(3), 1133. **[CrossRef]**

[13] Wang, W.; Li, C.; Li, Y.-Z.; Ruan, Y.; Wang, Z.; Fang, Y. Numerical Simulation of Jet Cooling Method Inside Air Gap in a High-Power Permanent Magnet Synchronous Motor. *Journal of Thermal Analysis and Calorimetry*, 2024, 149(12), 6095–6111. **[CrossRef]**

[14] Dai, Q.; Liu, X.; Huang, S. Analytical Calculation and Experimental Validation of 3D Rotor Eddy Current Loss in High-Speed Permanent Magnet Synchronous Motors. *IEEE Transactions on Industrial Electronics*, 2024, 71(11), 14569–14579. **[CrossRef]**



Qingyi Kong was a lecturer and master's supervisor at the School of Electrical Engineering at Hebei University of Science and Technology from 2014 to 2017. Since 2017, he has been a professor at Hebei Transportation Vocational and Technical College. From 2020 to the present, he has held the position of Technical Director at Mingzhi Electrical Appliances (Taicang) Co., Ltd. in Suzhou, China. He has published more than 30 articles and holds 17 patents. His main research interests include engineering electromagnetic field analysis, high-speed permanent magnet motor design, and the design and application of hydrogen fuel cell air compressors. Dr. Kong served as an IEEE member of the, a senior member of the Structural Health Monitoring and Early Warning Branch of the China Instrument and Control Society, a senior member of the China Electrotechnical Society, a senior member of the Hebei Electrical Engineering Society, and a peer reviewer for several academic journals.



Shengyan Zhou has been studying at Hebei Jiaotong Vocational and Technical College, in 2023. During this period, her research with the team has primarily focused on areas such as high-speed permanent magnet motors and unmanned cleaning vehicles.



Yuhui Fan has been studying at Hebei Jiaotong Vocational and Technical College, in 2023. During this period, her research with the team has primarily focused on areas such as high-speed permanent magnet motors and unmanned cleaning vehicles.



Zida Hao has been studying at Hebei Jiaotong Vocational and Technical College, in 2023. During this period, her research with the team has primarily focused on areas such as high-speed permanent magnet motors and unmanned cleaning vehicles.



Ye Rong was born in 1983 and received a master's degree in physics from Hebei Normal University in Shijiazhuang City, Hebei Province, China, in 2017. Obtain a doctoral degree in Optics and Electronic Engineering from the PLA Army Engineering University, in 2025. Since 2017, she has been working at Hebei Transportation Vocational and Technical College as a teacher in the electric power supply specialty. During her tenure, she has published more than ten articles, with her research primarily focusing on military optoelectronic system applications, few-shot image processing, and visual image processing, high-speed permanent magnet motors, uncrewed sweeping vehicles.